
**PX912: MULTISCALE MODELLING METHODS
AND APPLICATIONS II - SOLIDS COURSEWORK
REPORT**

Name: Jacob Eller
Student ID: 1738743

The University of Warwick
Department of Physics

February 2023

Abstract

Abstract In this work I used finite element methods (FEM) to investigate how the material depicted in Figure 1 is affected if the specified loads are applied to it. I wrote a program in Python 3 that allowed me to calculate nodal displacements and by extension element strains, stresses and Von Mises stresses. I implemented several different densities of nodes to observe how this affected the values calculated. I found that as nodal density increased, the calculated values converged significantly to give increasingly accurate approximations of the true values. The deformation was found to be elastic, not plastic.

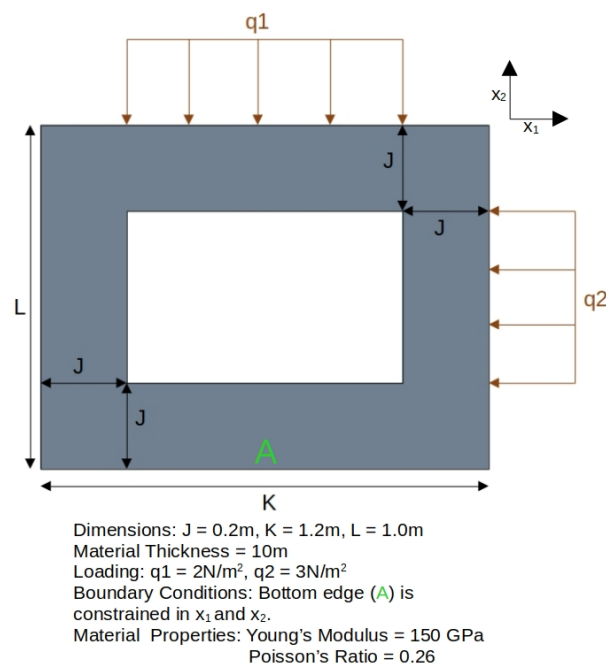


Figure 1: Schematic of the studied system. Includes material dimensions, material properties and loading.

1 Introduction

Finite element methods (FEM) are numerical techniques used in many fields of engineering, including fluid mechanics [1], mechanical engineering [2] and chemical engineering.[3] They are used to obtain approximate solutions to complex differential

equations. These numerical solutions generally correspond to solution fields (i.e. how properties vary over space/time), so FEM can often be employed to offer affordable computation of properties at specific spatial/temporal points.[4]

In this work I applied FEM using computational techniques to calculate the nodal displacements, element strains, stresses and Von Mises stresses associated with the material and loading defined in figure 1. I wrote the program in Python 3.0, without the use of any public FEM libraries. I investigated how the calculated values of these properties varied with the number of elements/domains a material was divided into. I found that as the number of elements increased, the values calculated converged significantly to give increasingly accurate approximations of the true values. The deformation was found to be elastic, not plastic.

2 Theory and Methodology

2.1 Foundations of FEM

Most FEM share the same basic blueprint. The domain over which the differential equation(s) of interest apply must be divided into a number of elements, defined by a mesh of nodes.

When attempting to solve for a particular property/solution field, there is a corresponding ‘strong form’. This is a set of higher order governing differential equations that describe the behaviour of the material. The term ‘strong form’ stems from the fact that the the solution of these higher order equations must be differentiable to this high order at all points. Finding approximate solutions with FEM that satisfy this requirement is not trivial, so generally a ‘weak form’ is derived instead.

The weighted-residual method can be used to generate the weak form; this involves integrating the product of the strong form and a test function over the domain where the differential equations apply. The weak form features lower order differentials than the strong form, which results in looser restrictions on the solutions in terms of higher order differentiability. This is more amenable for use in FEM as it allows greater flexibility in the basis functions used to generate the approximate solution field. These basis functions are known as ‘shape functions’, and they are used to form the exact solution of the weak form. This exact solution takes the form $u^h(x) = \sum_i N_i(x) d_i$, where N_i is a shape function corresponding to node i and d_i is the value of the solution field at node i . For different solution fields, various techniques are required to calculate the nodal degrees of freedom that must be fed into the FEM framework. These shape functions interpolate between the values for the solution field at these nodes, offering an approximation of the continuous solution field.

Often, a system's geometry/coordinates and solution fields can be effectively interpolated by shape functions of the same polynomial order. In these instances, the isoparametric concept applies: $\underline{N}_u = \underline{N}_g$, where \underline{N}_u is the vector of shape functions used to interpolate nodal degrees of freedom and \underline{N}_g is the vector of shape functions used to interpolate nodal coordinates.

2.2 General Approach

The approach I used in this work was to calculate displacements at defined nodal points using the mathematical relationship $\underline{K}\underline{d} = \underline{f}$, where \underline{K} is the global stiffness matrix, \underline{d} is the nodal displacement vector and \underline{f} is the nodal force vector. I then used these nodal displacements to calculate element strains and stresses. This FEM methodology allowed me to approximate the solution field corresponding to the displacement of material points under the specified loads. To calculate the solution field analytically would have required the solution of the equilibrium equation (the strong form); $\nabla \cdot \sigma + b = 0$, where σ is the Cauchy stress tensor and b corresponds to body forces.

2.3 Plane Strain Conditions

As can be seen in Figure 1, the material of interest has a thickness (10m) that is significantly greater than the other two dimensions of the 3D object. This permits the use of the 'plane strain' approximation, which involves making the assumption that the two dimensions of shorter lengths are constrained, whilst the third is unconstrained. This approximation stems from the idea that any displacements in the ' x_3 ' dimension will likely be negligible, meaning any strains and stresses in this direction can be neglected. Plane strain conditions result in the mesh of nodes - and their corresponding degrees of freedom - only having to be defined/calculated in the x_1x_2 -plane. This greatly reduced the computational cost associated with this study. This approximation also leads to a reduction in the size of the matrix of elastic constants and the Voigt stress and strain vectors; the assumption of zero strain in the x_3 dimension also means the corresponding stresses are zero. The resulting Voigt tensors are;

$$\begin{pmatrix} \sigma_{11} \\ \sigma_{22} \\ \sigma_{12} \end{pmatrix} = \frac{E}{(1+\nu)(1-2\nu)} \begin{pmatrix} 1-\nu & \nu & 0 \\ \nu & 1-\nu & 0 \\ 0 & 0 & \frac{1-2\nu}{2} \end{pmatrix} \begin{pmatrix} \epsilon_{11} \\ \epsilon_{22} \\ 2\epsilon_{12} \end{pmatrix} \quad (1)$$

where E and ν correspond to the Young's modulus and Poisson's ratio of the material

respectively. The left hand term is the Voigt stress tensor, the linear elasticity matrix C is the middle term and the right hand term is the Voigt strain tensor.

2.4 Meshing

I divided the material of interest into many smaller elements by generating a uniform grid of nodes across the material in the $x_1 x_2$ -plane. As the surface area of individual elements tends to zero, the data obtained from their study should converge towards data that would be obtained from an analytical solution. This is because an increase in the density of nodes/element reduces the distance between calculated values over which we must interpolate, which inherently increases the accuracy of the results. To gain an understanding of how the error resulting from finite element discretization would vary with the density of nodes, I generated five meshes with differing nodal densities (Figure 5, Appendix 1.1). With each subsequent mesh, the number of elements in each dimension doubled, meaning the number of elements in the material quadrupled.

2.5 Shape Functions

The topologies of the meshes (Figure 5, Appendix 1.1) generated for the system of interest are uniform and regular - this suggests that the use of the isoparametric concept is valid in this scenario. Hence, I chose to generate shape functions for the four nodes defining each element through consideration of the nodal coordinates. As illustrated in Figure 2, I used natural coordinates (ξ, η) rather than using physical coordinates (x_1, x_2) explicitly; defining shape functions in natural coordinates generally simplifies the resulting shape functions and thus the process of integrating/differentiating said functions. The use of natural coordinates will not have led to any significant reduction in complexity in this research because all elements were regular squares, but I chose to use this method to improve the transferability of my code to less uniform systems. Shape functions must be unity at the node to which they are associated and equal to zero at all other nodes, which makes their derivation trivial. The resulting shape functions for all four nodes of each element are of the form; $N_i^e = \frac{1}{4}(1 + \xi_i \xi)(1 + \eta_i \eta)$, with the index i corresponding to the i 'th node in the element (following the number scheme in Figure 2) and ξ_i and η_i are the natural coordinates of the i 'th node.

2.6 Boundary Conditions

Correctly implementing boundary conditions was imperative to ensuring the validity of my calculations. One such condition was that the bottom edge ('A' in Figure 1) of

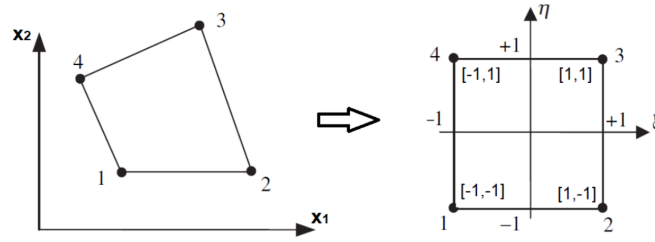


Figure 2: Illustration of the mapping of physical coordinates onto natural coordinates.

the material was constrained in both x_1 and x_2 . I incorporated this into the nodal displacement vector (\underline{d}) by fixing all elements corresponding to the nodes in the bottom edge as zero. The second boundary condition was the loading of the system. There was one load applied parallel to each axis (x_1 and x_2). The load applied parallel to the x_1 axis (denoted 'q2' in Figure 1) was a pressure of 3 N/m^2 . The surface area of the region to which this was applied was 6 m^2 , meaning the force applied to this region was 18 N . The load applied parallel to the x_2 axis (denoted 'q1' in Figure 1) was a pressure of 2 N/m^2 . The surface area of the region to which this was applied was 8 m^2 , meaning the force applied to this region was 16 N . These forces were uniform, so the magnitudes of forces applied to nodes in the relevant regions were equal to the negatives (specifying direction) of the total forces divided by the number of nodes experiencing these forces. This was incorporated into the force vector (\underline{f}) by setting these values of forces for the relevant elements. Examples of the resulting vectors (\underline{d} and \underline{f}) are in Appendix 1.2.

2.7 Strain Displacement Matrices

Strain-displacement matrices in FEM relate the strains in a material's elements to nodal displacements. They are essential for the calculation of the global stiffness matrix, and thus nodal displacements. The matrices for each element can be calculated from the Jacobian matrix (\underline{J}^e) and the natural coordinate strain-displacement matrix (\underline{B}_n^e):

$$\underline{J}^e = \begin{pmatrix} \frac{\partial N_1^e}{\partial \xi} & \frac{\partial N_2^e}{\partial \xi} & \frac{\partial N_3^e}{\partial \xi} & \frac{\partial N_4^e}{\partial \xi} \\ \frac{\partial N_1^e}{\partial \eta} & \frac{\partial N_2^e}{\partial \eta} & \frac{\partial N_3^e}{\partial \eta} & \frac{\partial N_4^e}{\partial \eta} \end{pmatrix} \begin{pmatrix} c_{1(1)}^e & c_{2(1)}^e \\ c_{1(2)}^e & c_{2(2)}^e \\ c_{1(3)}^e & c_{2(3)}^e \\ c_{1(4)}^e & c_{2(4)}^e \end{pmatrix}, \quad \underline{B}_n^e = \begin{pmatrix} \frac{\partial N_1^e}{\partial \xi} & \frac{\partial N_2^e}{\partial \xi} & \frac{\partial N_3^e}{\partial \xi} & \frac{\partial N_4^e}{\partial \xi} \\ \frac{\partial N_1^e}{\partial \eta} & \frac{\partial N_2^e}{\partial \eta} & \frac{\partial N_3^e}{\partial \eta} & \frac{\partial N_4^e}{\partial \eta} \end{pmatrix},$$

where N_i^e corresponds to the shape function associated with node i of element e , and $c_{j(i)}^e$ corresponds to the physical x and y ($j = 1$ and 2 respectively) coordinates of node i

in element e . The strain-displacement matrices for each element ($\underline{\underline{B}}^e$) can be calculated in this way;

$$\underline{\underline{B}}^e = (\underline{\underline{J}}^e)^{-1} \underline{\underline{B}}_n^e = \begin{pmatrix} \frac{\partial N_1^e}{\partial x_1} & \frac{\partial N_2^e}{\partial x_1} & \frac{\partial N_3^e}{\partial x_1} & \frac{\partial N_4^e}{\partial x_1} \\ \frac{\partial N_1^e}{\partial x_2} & \frac{\partial N_2^e}{\partial x_2} & \frac{\partial N_3^e}{\partial x_2} & \frac{\partial N_4^e}{\partial x_2} \end{pmatrix}$$

Due to my system being divided into four-node two-dimensional elements, it must be written in the form shown in Appendix 1.3 for upcoming calculations.

2.8 Global Stiffness Matrices

The global stiffness matrix (mentioned in section 2.2) is formed by overlaying element stiffness matrices corresponding to all elements in the material. To calculate the element stiffness matrices analytically requires taking a definite integral over the domain of the element, which I approximated numerically using a Gauss Quadrature;

$$\underline{\underline{k}}^e = t \int_{-1}^1 \int_{-1}^1 \underline{\underline{B}}^{eT} \underline{\underline{C}} \underline{\underline{B}}^e \det \underline{\underline{J}}^e d\xi d\eta \approx t \sum_{i=1}^{n_\xi} \sum_{j=1}^{n_\eta} w_i w_j \underline{\underline{B}}^{eT}(\xi_i, \eta_j) \underline{\underline{C}} \underline{\underline{B}}^e(\xi_i, \eta_j) \det \underline{\underline{J}}^e(\xi_i, \eta_j),$$

where t is the material thickness (10 m), $\underline{\underline{k}}^e$ is the element stiffness matrix, $\underline{\underline{C}}$ is the linear elasticity matrix (section 2.3), w_i and w_j are weights and n_ξ and n_η are the number of values of ξ and η that define the integration points. The weights and integration points I used are summarised in Appendix 1.4, Table 1. $\underline{\underline{B}}^e(\xi_i, \eta_j)$ and $\underline{\underline{J}}^e(\xi_i, \eta_j)$ are the strain displacement and Jacobian matrices calculated with the natural coordinates of the integration points as inputs.

To construct the global stiffness matrix, the element stiffness matrices had to be overlaid so that elements corresponding to the same global node in different matrices were summed. The `np.ix_` function proved useful for this purpose.

2.9 Nodal Displacements

Using the relationship; $\underline{\underline{K}} \underline{\underline{d}} = \underline{\underline{f}}$, calculation of displacements is possible. The associated computational cost can be minimised by using reduced forms of $\underline{\underline{K}}$ and $\underline{\underline{f}}$. These reduced forms originate from the boundary condition specifying that nodes on the bottom edge (denoted 'A' in Figure 1) were constrained in both the x_1 and x_2 dimensions. A known nodal displacement of zero means that any elements of $\underline{\underline{K}}$ and $\underline{\underline{f}}$ that contribute to generating the displacements of these nodes can be neglected, leading to a significant reduction in their sizes. Using these reduced tensors I calculated the corresponding

reduced nodal displacement vector. I did this using the 'linalg.solve' function from the numpy library to avoid the issues of numerical instability associated with direct matrix inversion.

2.10 Strains, Stresses and the Von Mises Formalism

Using the framework built in prior sections, it was then possible to calculate the Voigt strain tensor in each element at each of the 'integration points' (Appendix 1.4, Table 1) used in the Gauss quadrature in section 2.8; $\underline{\epsilon}_{IP}^e(\xi_i, \eta_j) = \underline{B}^e(\xi_i, \eta_j) \underline{d}^e = (\epsilon_{11}^e \ \epsilon_{22}^e \ \epsilon_{12}^e)^T$, where ϵ_{IP}^e corresponds to the Voigt strain tensor for element e at the integration point with natural coordinates (ξ_i, η_j) . This then allowed the Voigt stress tensor at each integration point ($\underline{\sigma}_{IP}^e$) to be calculated using the relationship in (1). The total stress tensor for each element ($\underline{\sigma}^e$) was calculated from these Voigt stress tensors;

$\underline{\sigma}^e = \sum_{IP=1}^{n_G} \sigma_{IP}^e \det J_{IP}^e w_{IP}$, where n_G is the number of integration points. The total strain tensor for each element ($\underline{\epsilon}^e$) was calculated in a similar manner; $\underline{\epsilon}^e = \sum_{IP=1}^{n_G} \epsilon_{IP}^e \det J_{IP}^e w_{IP}$.

To allow the comparison of the magnitude of stresses calculated with different nodal densities, it was logical to generate a scalar measure of stress. Thus I calculated the Von Mises stress (VMS) for each element, which scales with the magnitude of stress in all dimensions. VMS is defined as a function of the elements of the three dimensional Voigt stress tensor;

$$VMS = \sqrt{\frac{(\sigma_{11} - \sigma_{22})^2 + (\sigma_{22} - \sigma_{33})^2 + (\sigma_{33} - \sigma_{11})^2 + 6(\sigma_{21}^2 + \sigma_{22}^2 + \sigma_{23}^2)}{2}},$$

where all terms with an index including '3' correspond to stress components with contributions in the x_3 dimension. As discussed in section 2.3, by applying the plane strain approximation I have made the assumption that any strains in the x_3 dimension are insignificant and can be neglected. Thus, in my calculations of VMS, any terms corresponding to stress in x_3 were fixed at zero.

3 Results and Discussion

3.1 Nodal Displacements

Nodal displacements for all five nodal meshes were calculated. The resulting distortions to the material's geometry are illustrated in Appendix 1.5, Figure 6. All calculated nodal displacements were very small ($< 10^{-9}m$). This was expected as the system had an

incredibly high Young's modulus, which is a measure of a material's ability to resist elastic deformation under loading. The greatest nodal displacements for all meshes were surrounding the node at (0cm,1cm) relative to the origin defined in Appendix 1.5, Figure 6. This was also expected due to the bottom edge (A in Figure 1) being constrained in both x_1 and x_2 , and the pressure 'q2' acting in the direction of the origin. As can be seen in Figure 3, the magnitude of the maximum absolute displacement converged as the number of elements increased - this was unsurprising. When a material is divided into a small number of elements, the corresponding mesh is relatively sparse, with nodes relatively far away from one another. This leads to a less refined domain than would be available with a more dense mesh. As a result, a sparser grid is unlikely to capture complexities associated with the geometry/material properties as well as a finer grid. Thus, calculations with a sparser grid will be less likely to accurately determine the properties/character of the material. This logic aligns with the observed trend of convergence to a maximum nodal displacement of $\sim 2.9 \times 10^{-10}$ m as the number of elements increases. The values of maximum calculated nodal displacements, as well as their associated error relative to the highest density grid calculation is in Appendix 1.6, Table 2.

Of course, one cannot escape the fact that FEM approximates a continuous field by interpolating between discrete points. Thus, for all finite element analysis, there will be some associated finite element discretization error (FEDE). Theoretically, as the number of elements tends to infinity, the FEDE will tend towards zero. Therefore, the degree to which the accuracies of calculated nodal displacements are affected by FEDE, can be inferred from the extent to which the calculated values have been converged with

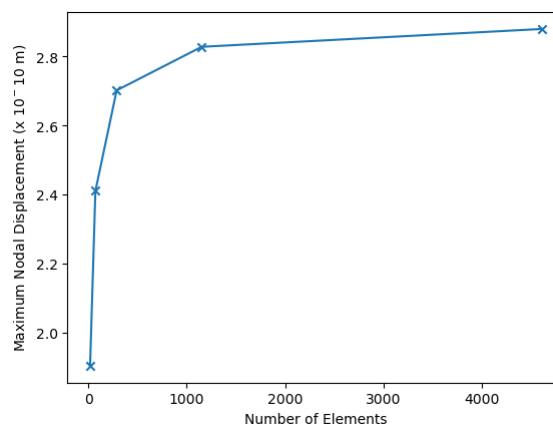


Figure 3: Values of maximum absolute nodal displacements calculated for various meshes with different numbers of uniform elements.

respect to the number of elements. Figure 3 suggests that for my system, the mesh with 4608 elements offers a high level of convergence. This indicates that the effect of FEDE on the accuracy of this result should be minimal.

3.2 Strains and Linear Elasticity

All materials have an associated yield strain, which is the amount of strain the material can undergo before deformation ceases to be elastic, and starts to be plastic. This can be interpreted qualitatively to mean that when a material undergoes a strain greater than the yield strain, some form of permanent deformation will occur. Whilst it is difficult to accurately predict the value of the yield strain, if strains are below a certain threshold ($\sim 10^{-3}$), it is generally safe to assume the material is experiencing elastic deformation. From the elemental Voigt strain vectors calculated for each mesh density, I extracted the maximum absolute values. I found that as the number of elements increased, the value of the maximum strain element converged (Appendix 1.7, Table 3, Figure 7) to approximately 5×10^{-14} , which indicates this material is certainly undergoing elastic deformation, not plastic deformation.

3.3 Von Mises Stresses

As mentioned in section 2.10, Von Mises stresses are scalar quantities that are useful in the simplification of the comparison of the magnitude of stresses, which are physically represented by a multidimensional stress tensor. Plots illustrating the Von Mises stresses calculated for each element in each meshing design are displayed in Appendix 1.8, Figure 8. The distribution of stresses across all of the meshes showed significant agreement. The areas of highest stress were clearly shown to be around the physical coordinates (1.0 cm, 0.2 cm), (0.2, 0.8 cm), (0.2 cm, 0.2 cm) and (0.1 cm, 0.2 cm), relative to the origin on the plots. This would be expected as the first three points are in the inside corners of the rectangle, where the loading of 'q1' and 'q2' will cause sudden and severe changes in geometry. The final point is situated at the left-hand edge of the material very close to the constrained bottom edge of the material. This proximity to the constrained region, combined with the fact that the directions of the loading forces combine to deform the material towards the bottom left corner, explain the high stress.

From the calculations carried out on the system with the five different meshing grids, I extracted the Von Mises stress with the greatest magnitude for each mesh. Figure 4 shows that as the number of elements increases, the size of strains decreases - converging to $\sim 0.01 N/m^2$. This convergence can be explained by consideration of the surface area of each element. In the more coarse meshes, the surface area covered by each individual

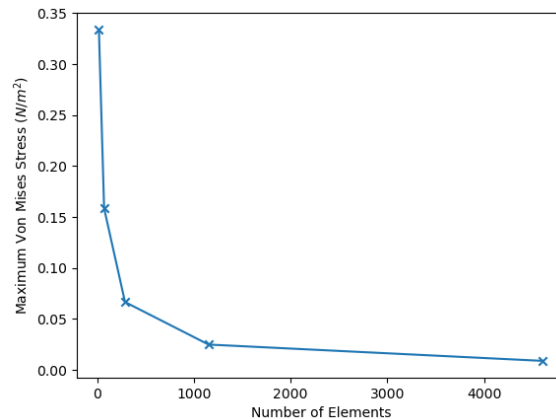


Figure 4: Values of maximum Von Mises stresses calculated for various meshes with different numbers of uniform elements.

element is larger than the finer meshes. The total stress tensors calculated for each element were dependent on the stresses calculated at the four integration points within an element. In large elements, the distance between these integration points in physical space is greater, making it more likely that the stress environment/concentration at each point will be very different. Thus, the total stress calculated for these elements will not accurately capture local variations in stress. It will instead average the stress over the large element, providing no information about local stress, which introduces inaccuracy into the resulting stress field. Conversely, with finer grids, the integration points will be closer in physical space and so will capture local variations in stress, which generates a more accurate stress field. Hence, error in stress calculation decreased as the number of nodes in meshes increased (Appendix 1.8, Table 4).

4 Conclusion

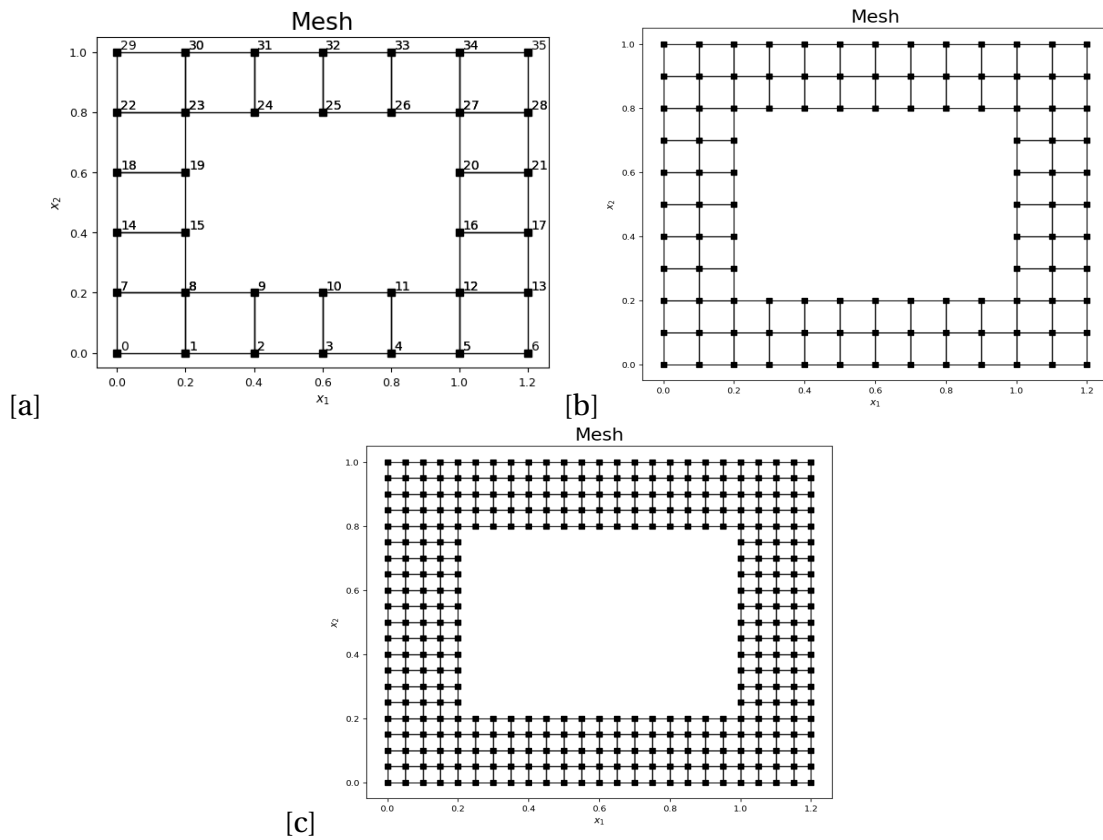
In this work I calculated approximate nodal displacements and Von Mises stress fields for the system in Figure 1. I carried out mesh refinement with 5 meshes of differing nodal densities. This showed that an increase in nodal density leads to a convergence in calculated strain, stress and displacements, which corresponds to an increase in the accuracy of calculated values. I also determined that the system was undergoing elastic deformation.

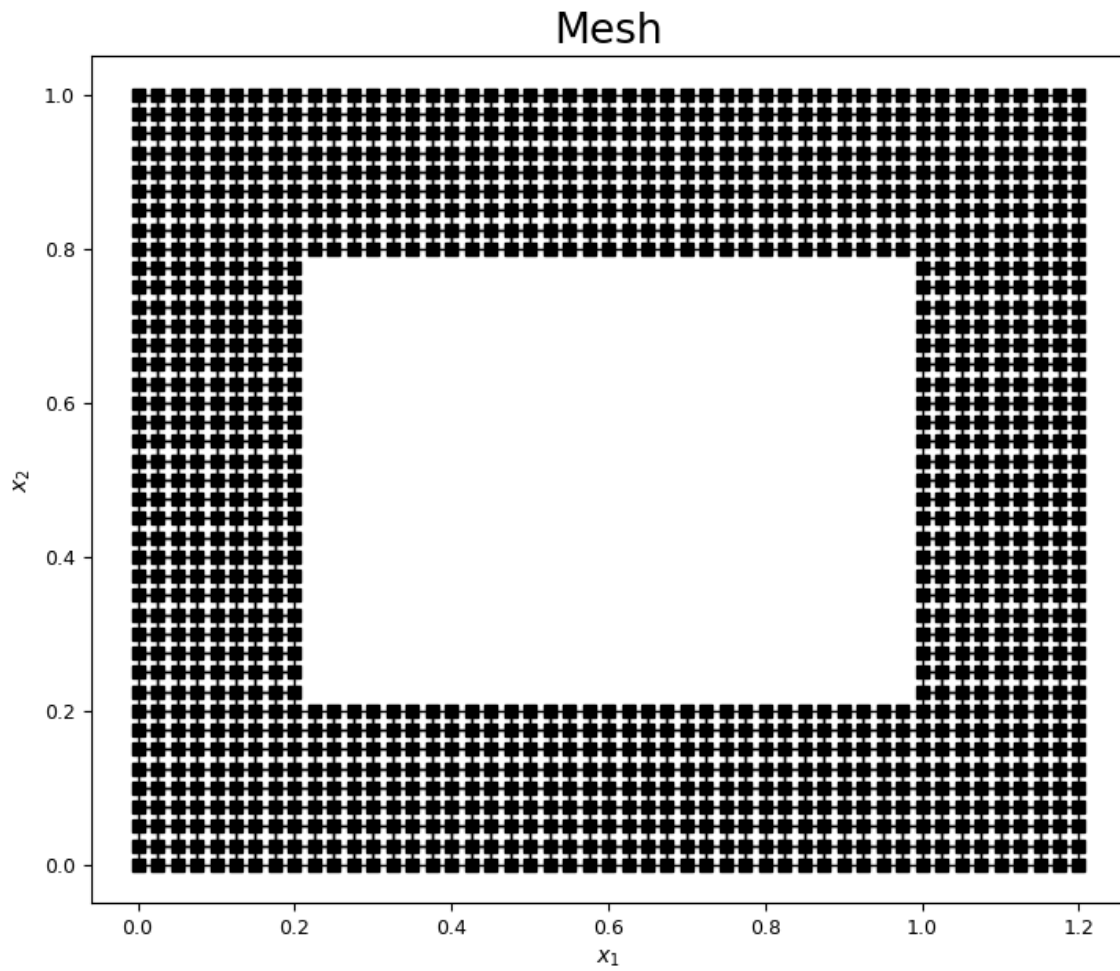
References

- [1] Olek C Zienkiewicz, Robert Leroy Taylor, and Perumal Nithiarasu. *The finite element method for fluid dynamics*. Butterworth-Heinemann, 2013.
- [2] Farzad Ebrahimi. *Finite Element Analysis: Applications in Mechanical Engineering*. BoD–Books on Demand, 2012.
- [3] P.L. Mills and P.A. Ramachandran. “Mathematical modelling of chemical engineering systems by finite element analysis using PDE/PROTRAN”. In: *Computers Mathematics with Applications* 15.9 (1988), pp. 769–794. ISSN: 0898-1221. DOI: [https://doi.org/10.1016/0898-1221\(88\)90129-0](https://doi.org/10.1016/0898-1221(88)90129-0). URL: <https://www.sciencedirect.com/science/article/pii/0898122188901290>.
- [4] Tirupathi Chandrupatla and Ashok Belegundu. *Introduction to finite elements in engineering*. Cambridge University Press, 2021.

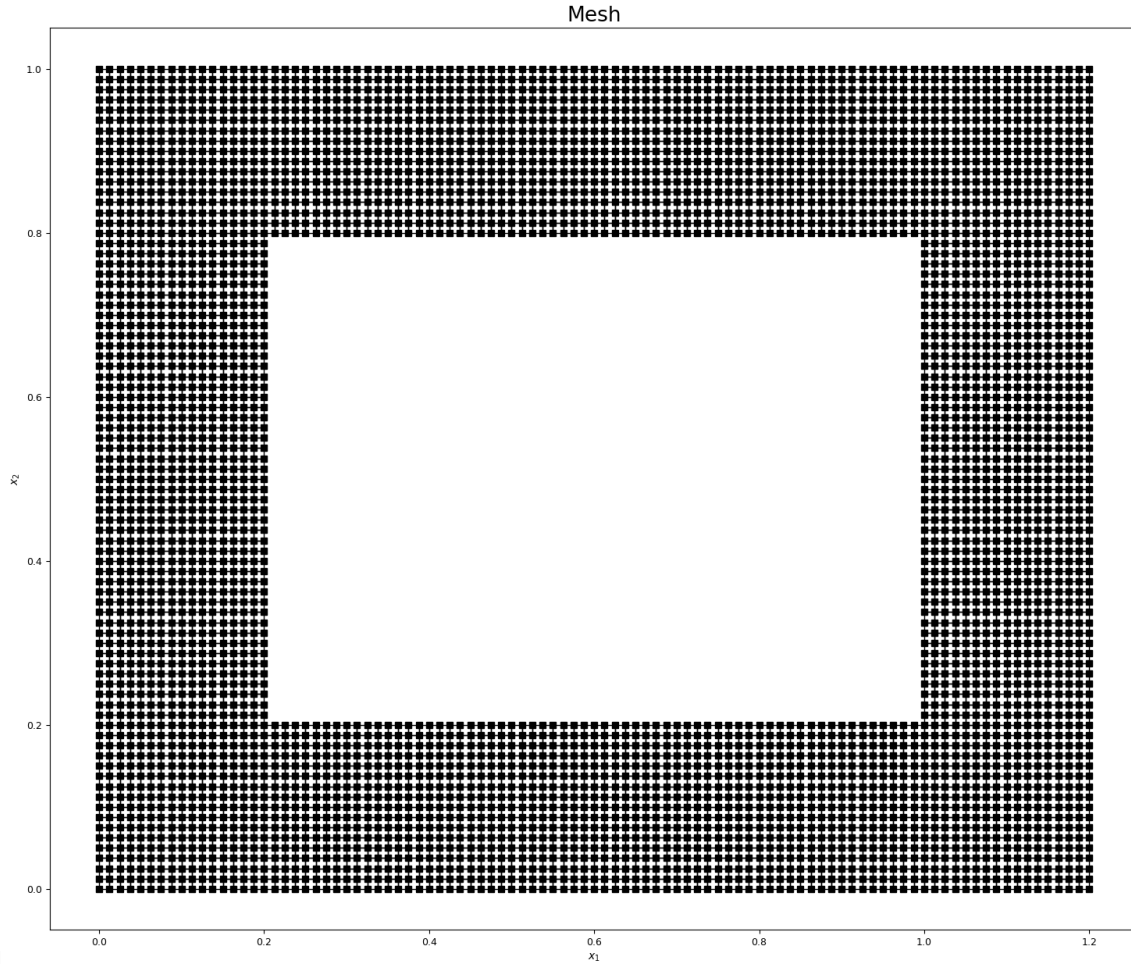
Appendices

Appendix 1.1





[d]



[e]

Figure 5: These are nodal meshes generated to discretize the domain of increasing nodal densities. Axes show physical coordinates in centimeters relative to the bottom left corner of the material in x_1x_2 -plane. Figure 5a) contains 18 elements. Figure 5b) contains 72 elements. Figure 5c) contains 288 elements. Figure 5d) contains 1152 elements. Figure 5e) contains 4608 elements

Appendix 1.2

$$\underline{d} = \begin{pmatrix} 0.0 & 0.0 & 0.0 & 0.0 & 0.0 & 0.0 & 0.0 & 0.0 & 0.0 \\ 0.0 & 0.0 & 0.0 & 0.0 & 0.0 & 1.0 & 1.0 & 1.0 & 1.0 \\ 1.0 & 1.0 & 1.0 & 1.0 & 1.0 & 1.0 & 1.0 & 1.0 & 1.0 \\ 1.0 & 1.0 & 1.0 & 1.0 & 1.0 & 1.0 & 1.0 & 1.0 & 1.0 \\ 1.0 & 1.0 & 1.0 & 1.0 & 1.0 & 1.0 & 1.0 & 1.0 & 1.0 \\ 1.0 & 1.0 & 1.0 & 1.0 & 1.0 & 1.0 & 1.0 & 1.0 & 1.0 \\ 1.0 & 1.0 & 1.0 & 1.0 & 1.0 & 1.0 & 1.0 & 1.0 & 1.0 \\ 1.0 & 1.0 & 1.0 & 1.0 & 1.0 & 1.0 & 1.0 & 1.0 & 1.0 \\ 1.0 & 1.0 & 1.0 & 1.0 & 1.0 & 1.0 & 1.0 & 1.0 & 1.0 \end{pmatrix}$$

$$\underline{f} = \begin{pmatrix} 0.0 & 0.0 & 0.0 & 0.0 & 0.0 & 0.0 & 0.0 & 0.0 & 0.0 \\ 0.0 & 0.0 & 0.0 & 0.0 & 0.0 & 0.0 & 0.0 & 0.0 & 0.0 \\ 0.0 & 0.0 & 0.0 & 0.0 & 0.0 & 0.0 & 0.0 & 0.0 & -4.5 \\ 0.0 & 0.0 & 0.0 & 0.0 & 0.0 & 0.0 & 0.0 & -4.5 & 0.0 \\ 0.0 & 0.0 & 0.0 & 0.0 & 0.0 & 0.0 & -4.5 & 0.0 & 0.0 \\ 0.0 & 0.0 & 0.0 & 0.0 & 0.0 & 0.0 & 0.0 & 0.0 & 0.0 \\ 0.0 & 0.0 & 0.0 & 0.0 & 0.0 & 0.0 & 0.0 & 0.0 & 0.0 \\ 0.0 & 0.0 & -4.5 & 0.0 & 0.0 & 0.0 & 0.0 & -3.2 & 0.0 \\ -3.2 & 0.0 & -3.2 & 0.0 & -3.2 & 0.0 & -3.2 & 0.0 & 0.0 \end{pmatrix}$$

These are the nodal displacement (\underline{d}) and nodal force (\underline{f}) vectors with boundary conditions applied (as specified in section 2.6). These are presented as 2-dimensional matrices due to a lack of space on the page, but should actually be interpreted as 1-dimensional vectors. Elements with odd indices correspond to the property in the x_1 dimension, and all others correspond to the property in the x_2 dimension.

Appendix 1.3

$$B^e = \begin{pmatrix} \frac{\partial N_1^e}{\partial x_1} & 0 & \frac{\partial N_2^e}{\partial x_1} & 0 & \frac{\partial N_3^e}{\partial x_1} & 0 & \frac{\partial N_4^e}{\partial x_1} & 0 \\ 0 & \frac{\partial N_1^e}{\partial x_2} & 0 & \frac{\partial N_2^e}{\partial x_2} & 0 & \frac{\partial N_3^e}{\partial x_2} & 0 & \frac{\partial N_4^e}{\partial x_2} \\ \frac{\partial N_1^e}{\partial x_2} & \frac{\partial N_1^e}{\partial x_1} & \frac{\partial N_2^e}{\partial x_2} & \frac{\partial N_2^e}{\partial x_1} & \frac{\partial N_3^e}{\partial x_2} & \frac{\partial N_3^e}{\partial x_1} & \frac{\partial N_4^e}{\partial x_2} & \frac{\partial N_4^e}{\partial x_1} \end{pmatrix}$$

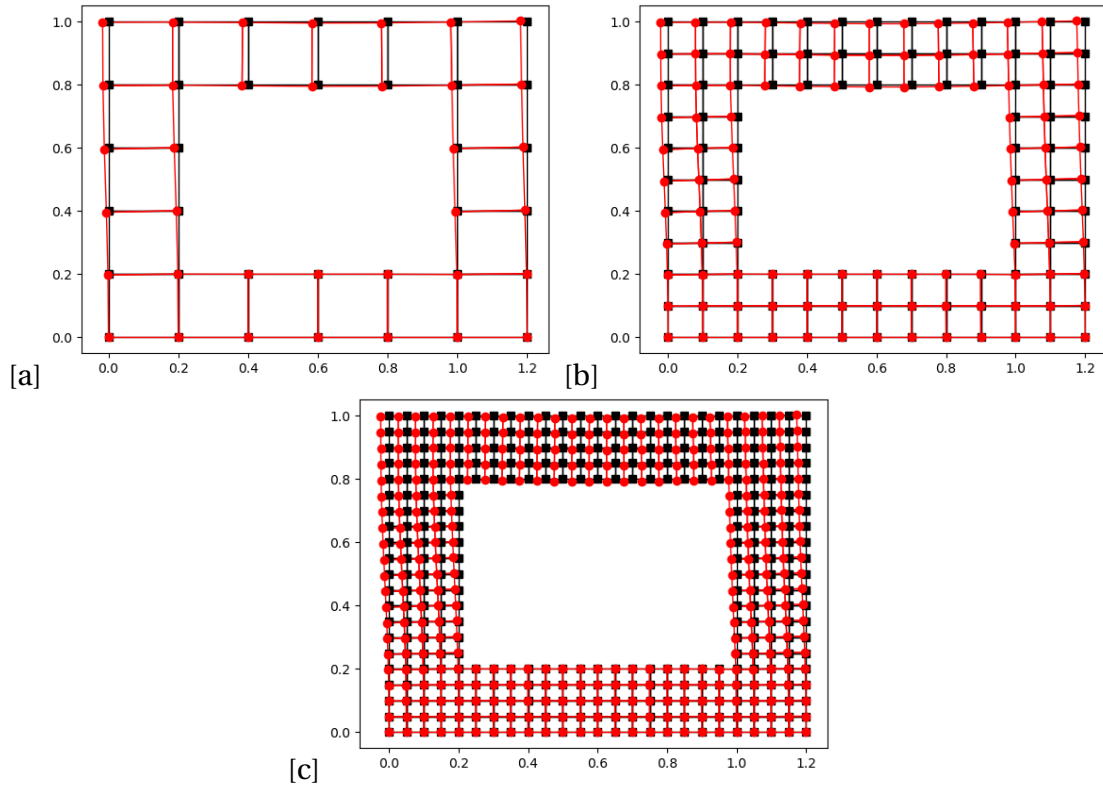
This is the form of the strain-displacement matrix used for all calculations after section 2.7.

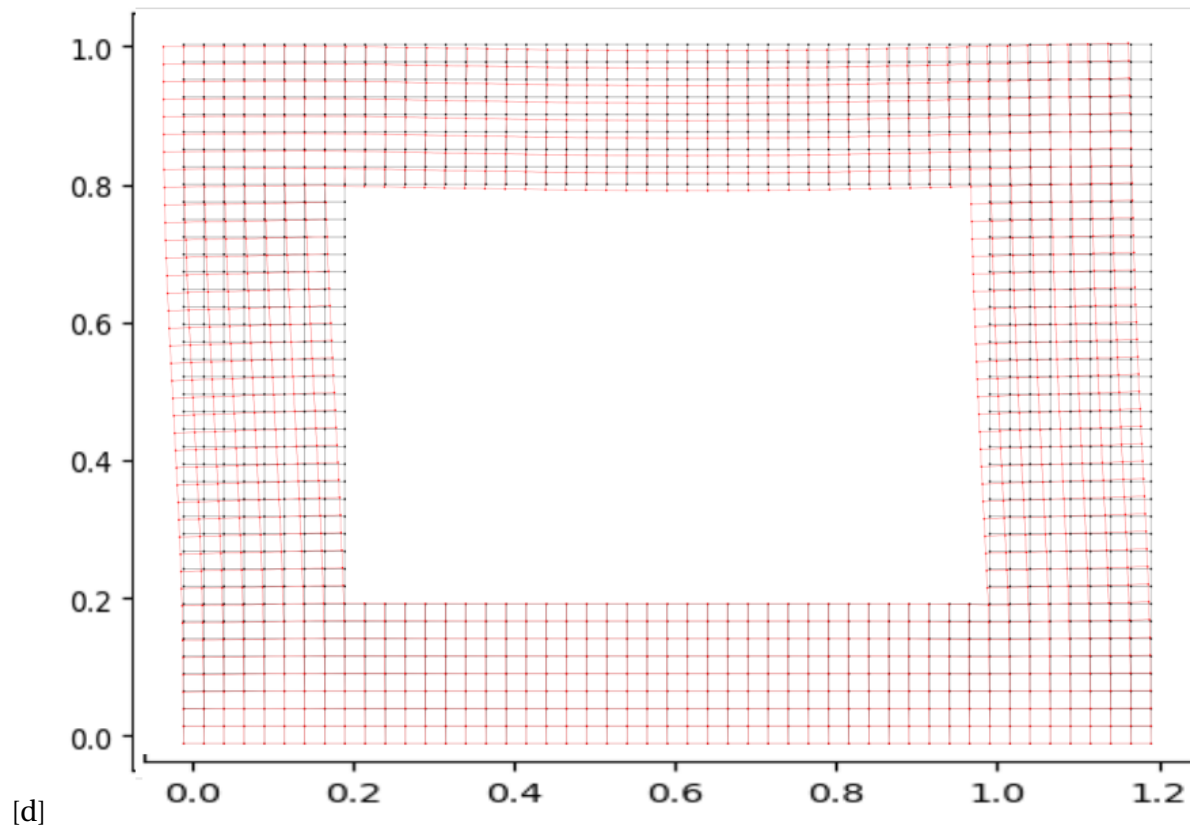
Appendix 1.4

Integration Point	η Coordinate	ξ Coordinate	Weight
1	$-\frac{1}{3}\sqrt{3}$	$-\frac{1}{3}\sqrt{3}$	1
2	$\frac{1}{3}\sqrt{3}$	$-\frac{1}{3}\sqrt{3}$	1
3	$\frac{1}{3}\sqrt{3}$	$\frac{1}{3}\sqrt{3}$	1
4	$-\frac{1}{3}\sqrt{3}$	$\frac{1}{3}\sqrt{3}$	1

Table 1: Table showing weights and coordinates for each integration point used in the Gauss quadrature to calculate element stiffness matrices.

Appendix 1.5





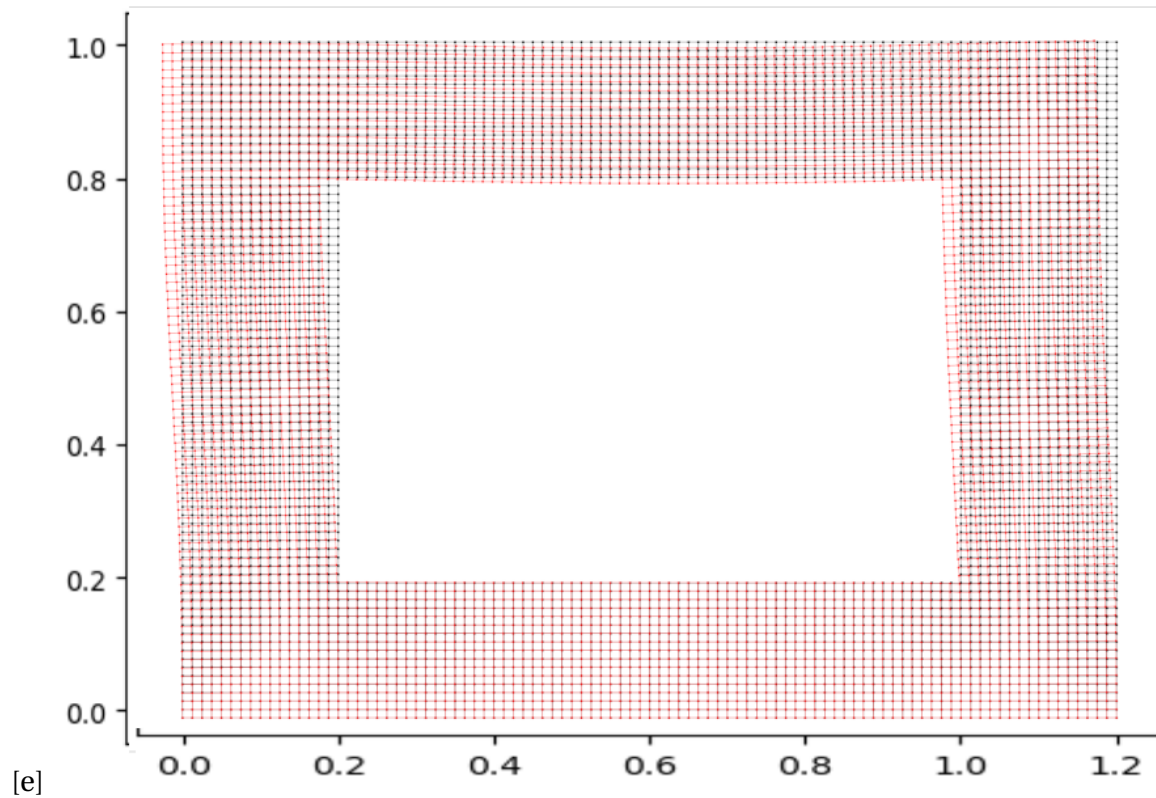


Figure 6: Nodal displacements calculated for meshes with different numbers of elements. The deformations are very slight, so their magnitudes were increased by a factor of 1,000,000. Figure 6a) contains 18 elements. Figure 6b) contains 72 elements. Figure 6c) contains 288 elements. Figure 6d) contains 1152 elements. Figure 6e) contains 4608 elements.

Appendix 1.6

No. of Elements	Max. Displacement ($\times 10^{-10}m$) (4.s.f)	Relative Error (%) (1.d.p)
18	1.903	33.9
72	2.410	16.3
288	2.702	6.2
1152	2.828	1.8
4608	2.880	N/A

Table 2: Table displaying the maximum displacement found for five different meshing designs, as well as the error in maximum displacement calculated for more sparse grids, relative to the most dense mesh.

Appendix 1.7

No. of Elements	Max. Strain Element ($\times 10^{-14}$) (2.d.p)
18	266.24
72	113.59
288	42.84
1152	15.25
4608	5.31

Table 3: Values of maximum absolute Voigt strain tensor elements calculated for various meshes with different numbers of uniform elements.

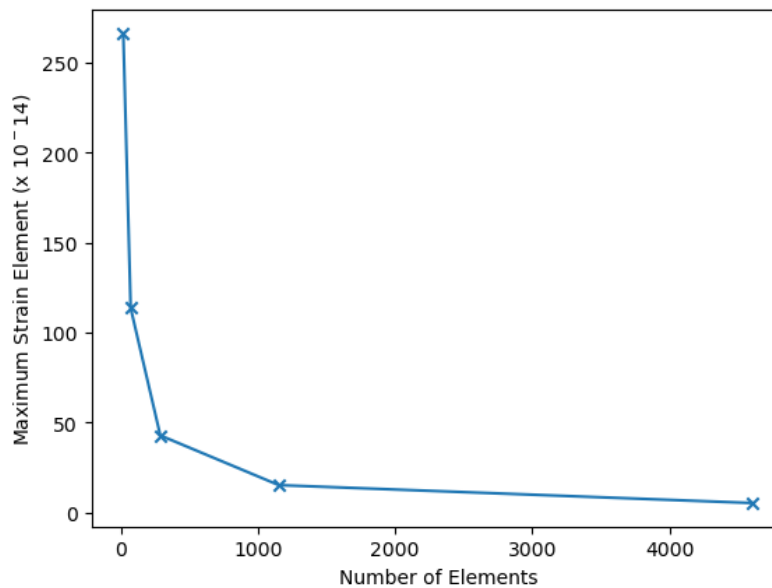
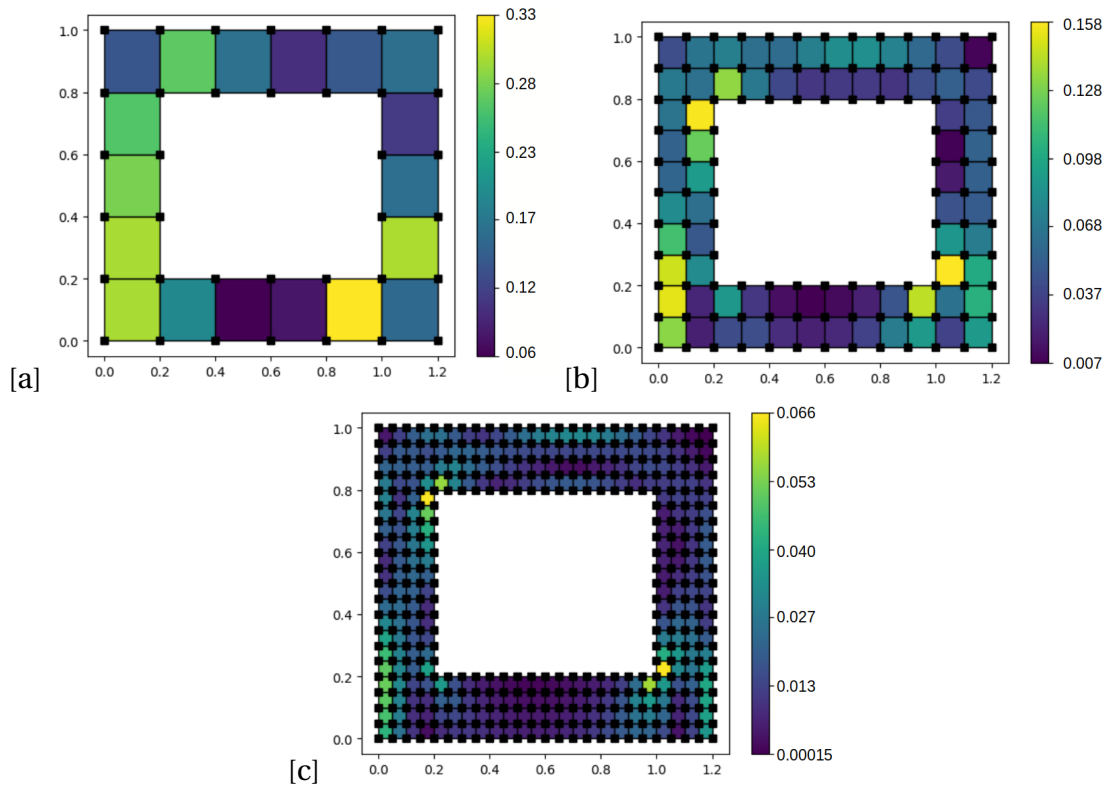
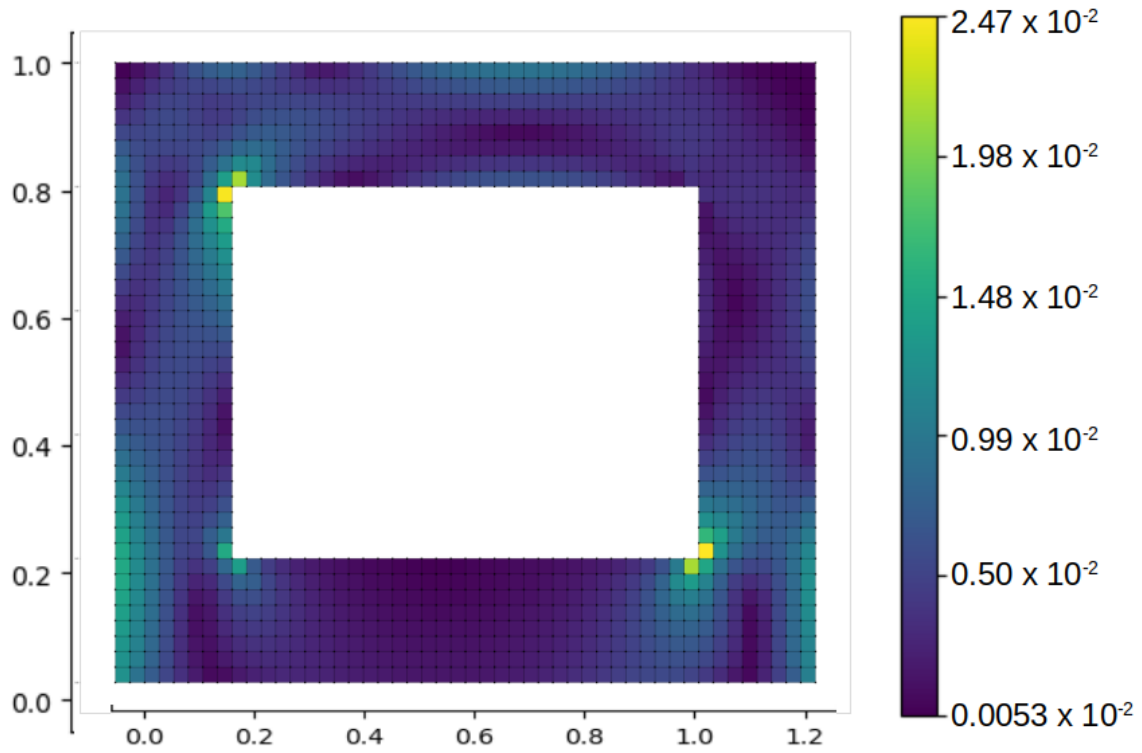
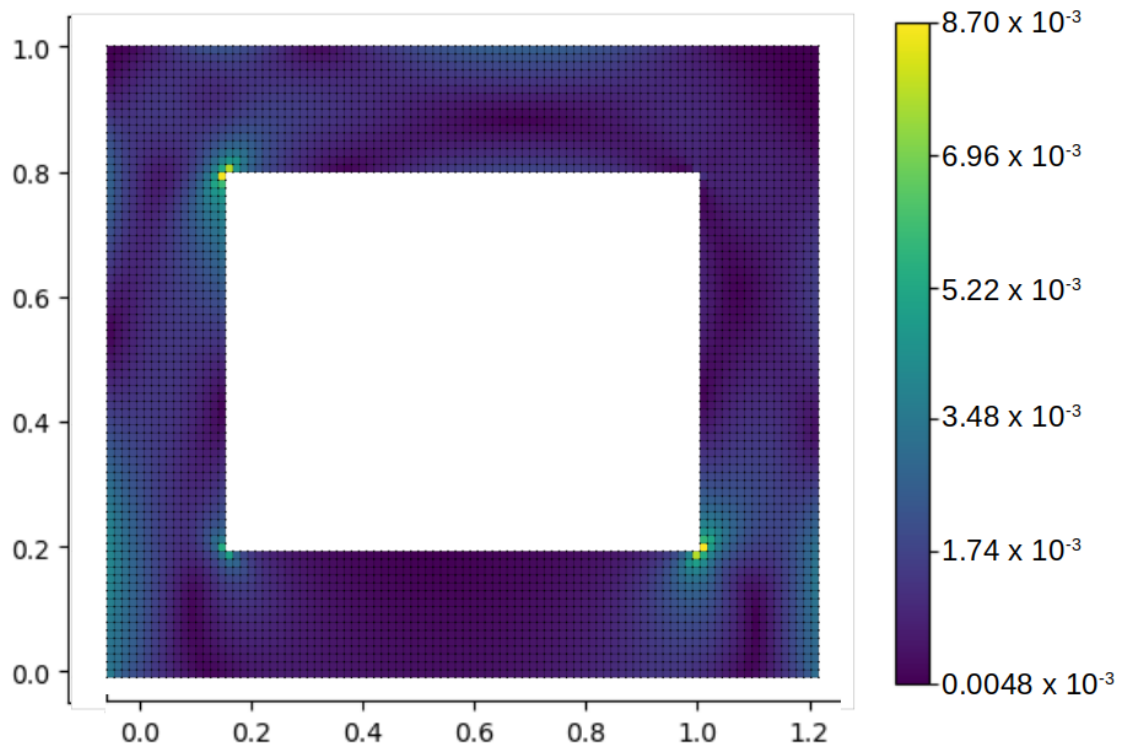


Figure 7: Convergence of values of maximum absolute Voigt strain tensor elements calculated for various meshes with different numbers of uniform elements.

Appendix 1.8



[d]



[e]

Figure 8: Colour map displaying the approximate Von Mises stress field calculated for each element, in each mesh design. Figure 8a) contains 18 elements. Figure 8b) contains 72 elements. Figure 8c) contains 288 elements. Figure 8d) contains 1152 elements. Figure 8e) contains 4608 elements.

No. of Elements	Max. Von Mises Stress (N/m^2 (2.s.f))	Relative Error (%) (1.d.p)
18	0.33	3736.1
72	0.16	1719.7
288	0.066	663.5
1152	0.025	183.98
4608	0.0088	N/A

Table 4: Table displaying the maximum Von Mises stresses found for five different meshing designs, as well as the error in maximum Von Mises Stress calculated for more sparse grids, relative to the most dense mesh.